Int. J. Electrochem. Sci., 17 **(2022)** Article Number: 221274, doi: 10.20964/2022.12.83

International Journal of
ELECTROCHEMICAL
SCIENCE
www.electrochemsci.org

Hard Carbon Derived from A New Type Resorcinol/2-Thenaldehyde Resin as High-Performance Anode Materials for Lithium-Ion Batteries

Qing Lu[1], *Lingqian Kong*[1,*], *Bo Liang*[2,*], *Jinsheng Zhao*[3]

[1] Dongchang colledge, Liaocheng University, Liaocheng, 252059, P.R. China
[2] School of Aviation and Transportation, Jiangsu College of Engineering and Technology, Nantong 226000, China
[3] Shandong Key Laboratory of Chemical Energy Storage and Novel Cell Technology, School of Chemistry and Chemical Engineering, Liaocheng University, Liaocheng, 252000, China.
[*]E-mail: lingqiankong@126.com (L.Q. Kong); bliang0325@163.com (B. Liang)

Received: 14 October 2022 / *Accepted:* 13 November 2022 / *Published:* 27 December 2022

In order to further improve the electrochemical properties of the resorcinol-formaldehyde (RF) resin and its derived hard carbon, a new D (electron donor)-D-A (electron acceptor) type resorcinol / 2-thenaldehyde (RT) resin was prepared by the high-temperature hydrothermal method using resorcinol and 2-thenaldehyde as raw materials. As lithium-ion electrode materials, RT resin and its derived hard carbon (HCs700) had significantly higher specific capacities than RF resin and its derived hard carbon, respectively. Compared with RF resin, RT resin had an extra thiophene unit in the molecule. The introduction of thiophene unit (donor unit) enabled RT resin to have a narrower band gap (Eg: 1.85 eV vs. 2 eV), better redox performance, and ultimately higher specific capacity. And the introduction of the thiophene unit caused the doping of N in HCs700, which greatly improved the electrochemical properties of the carbon material and greatly increased the number of active sites for the lithium-ion reaction. After 300 cycles, the capacities of RT resin, HCs700, and HCs700@GPE (graphene) at the current density of 100 mA g^{-1} were 270.1, 596.6, and 462.8 mAh g^{-1}, respectively. The prepared HCs700 and HCs700@GPE electrode materials had good specific capacity and rate performance, which were well suited as anode materials for lithium-ion batteries.

Keywords: Phenolic resin; Lithium-ion batteries; D-D-A type polymers; Conducting polymer

1. INTRODUCTION

In recent years, lithium-ion batteries (LIBs) have received widespread attention because of their light weight, high energy density, and low self-discharge rate [1, 2]. After commercialization, they have been widely used in the field of portable electronics, such as cell phones and computers [3, 4]. With the

rapid development of the electronic product, people have put forward higher requirements for the performance of LIBs [5]. Since electrode materials have a decisive influence on the electrochemical performance of LIBs, scientists have done a lot of research work on the electrode materials. The development of commercially available inorganic electrode materials has encountered bottlenecks due to their low specific capacity and single structure, and more and more researchers are turning their attention to organic electrode materials [6].

Organic electrode materials have the characteristics of easy synthesis and renewable resources, and more importantly, they can be designed and adjusted at the molecular level [7, 8]. Organic electrode materials mainly include organosulfur compounds [9, 10]], nitrogen-oxygen radicals [11, 12], organic carbonyl compounds [13-15], and conducting polymers [16, 17]. The first three organic electrode materials are easily dissolved in the electrolyte leading to a decrease in the capacity during cycling [18], while conducting polymers have a lower solubility in the electrolyte. Moreover, the composites of conducting polymers and carbon materials [19-21] have good electrical conductivity, which are suitable as electrode materials for LIBs [22, 23]. Copolymerization of electron donor (D) monomer and electron acceptor (A) monomer leads to the D-A type conducting polymer. The alternating arrangement of donor and acceptor units can significantly enhance the π-electron leaving domain [24], which greatly increases the intermolecular forces and facilitates the charge transport [25]. Not only that, D-A conducting polymers also have a narrow energy band gap (E_g) [26, 27], high conductivity, and low electrode potential, which are more suitable as anode materials for LIBs [28].

The resorcinol-formaldehyde (RF) resin was one of the D-A conducting polymers, which used the quinoid form of resorcinol as the electron acceptor unit and benzenoid form of resorcinol as the donor unit (as shown in Fig.1). Pekala [12] and Shiraishi [26] produced the RF resin by the condensation of resorcinol with formaldehyde under alkali catalysis by the low temperature hydrothermal method and high temperature hydrothermal method, respectively. RF resin can be used as electric double-layer capacitors [29] and LIBs electrodes [30, 31]. For example, Wang [32] investigated the effect of carbonization treatment conditions on the charge-discharge performance of LIBs prepared from the carbonized RF. The results showed that both the carbonization temperature and the specific surface area of the carbonized products were important factors affecting the electrochemical performance of LIBs, and the optimal resin carbonization temperature was obtained to be 700°C. J. Lu [33] used a melt blending method to disperse graphene(GPE) uniformly in the RF resin, and GPE greatly improved the electrical conductivity of the composite. When the GPE was added at 2%, the impedance of the composite was 140 Ω, and the impedance was reduced to 1/25 of that of the blank group. However, the reversible capacity of the RF resin and its derived hard carbon were found to be limited to 145 mAh g^{-1} at 100 mA g^{-1} [34-38] and 385 mAh g^{-1} at 37.2 mA g^{-1} [37], respectively.

In order to further improve the electrochemical properties of the RF resin and its derived hard carbon, this paper synthesized a new resorcinol / 2-thenaldehyde (RT) resin by the high-temperature hydrothermal method catalyzed by ammonia using resorcinol and 2-thenaldehyde as raw materials (as shown in Fig. 2). The reaction mechanism of synthesizing RT resin was the same as that of synthesizing RF resin [26]. As can be seen from Fig. 1 and 2, the RT resin synthesized in this paper was a D-D-A type conducting polymer, in which the electron donor unit was thiophene and the benzenoid form of resorcinol, and the electron acceptor unit was the quinoid form of resorcinol. Whereas the RF resin was

a D-A type conducting polymer, in which the electron donor unit and acceptor unit were the benzenoid and quinoid form of resorcinol, respectively.

Compared with RF resin, RT resin had the following advantages with the addition of the thiophene donor unit. On the one hand, the strong electron donating ability of the thiophene unit led to the lower LUMO (lowest unoccupied molecular orbital) energy level and higher HOMO (highest occupied molecular orbital) energy level of RT resin [39], and the redox ability of RT resin was enhanced for better lithium embedding and de-embedding [27, 40]. Moreover, the RT resin had a narrower E_g and a larger conductivity, improving its rate performance. On the other hand, the thiophene donor unit resulted in the enhanced coplanarity and conjugation effect of RT resin, and when lithium ions were inserted, the charge can be rapidly dispersed throughout the polymer backbone and quickly stabilized, which facilitated further embedding of subsequent lithium ions [41].

Furthermore, The RT resin derived hard carbon (HCs700) was obtained by the carbonization of RT resin at 700°C in this paper. Compared with RF resin derived hard carbon, HCs700 should have a higher specific capacity due to the fact that the former was an amorphous carbon while the latter was an N-doped amorphous carbon. After nitrogen doping, the replacement of carbon atoms by nitrogen changed the original crystal structure, affecting the spin density and charge distribution around the carbon atoms, thereby increasing the active sites on the surface of carbon materials, which was beneficial to the increase of specific capacitance [42, 43].

Finally, the morphology and structural characteristics of RT resin, Hcs700, and HCs700@GPE were investigated, and their electrochemical properties were also compared.

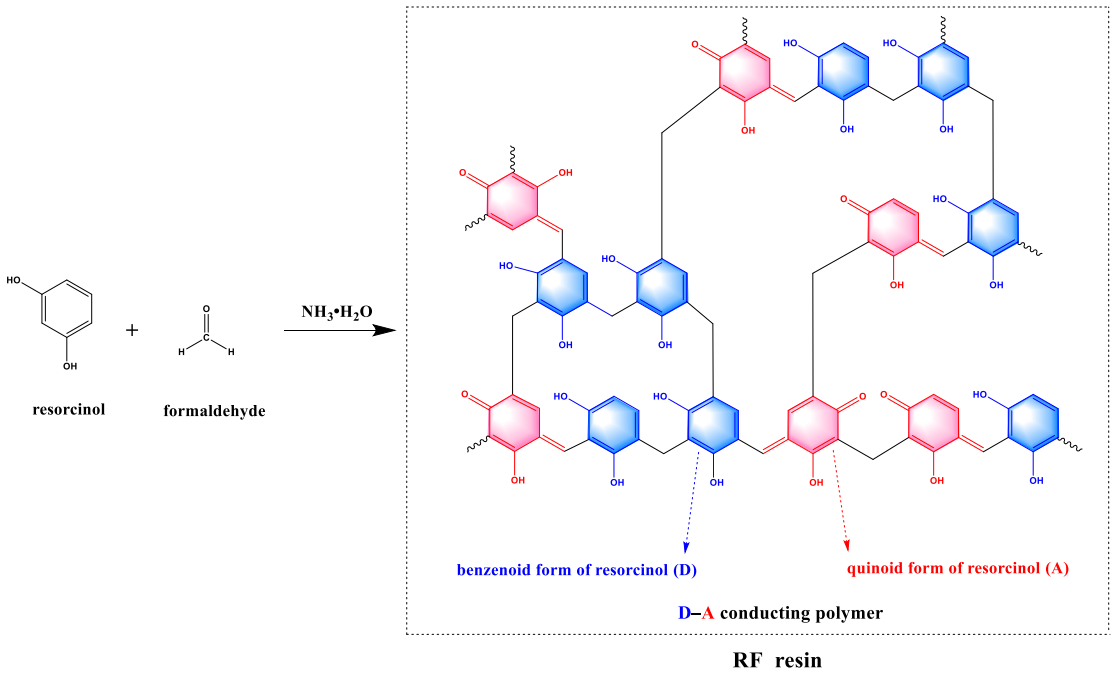

Figure 1. Schematic diagram of the structure of RF resin prepared by Yasuhiro Shiraishi[26] using resorcinol and formaldehyde as raw materials

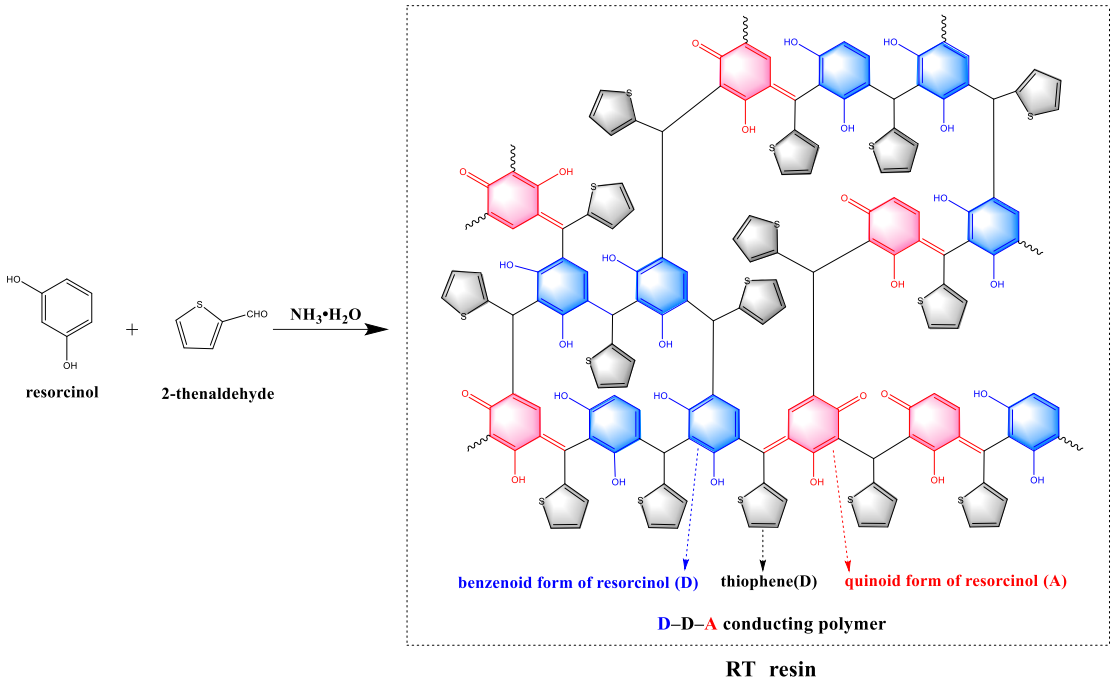

Figure 2. Schematic diagram of the structure of RT resin prepared from resorcinol and 2-thenaldehyde in this paper

2. EXPERIMENTAL SECTION

2.1. Materials

Anhydrous ethanol and acetone were bought from Yan Tai Far East Fine Chemical Co., Ltd. Graphene, aqua ammonia (25%) and 1-methyl-2-pyrrolidinone (NMP, 99.9%) were purchased from Aladdin Chemical Co., Ltd China. 2-thenaldehyde (98.0 %) was bought from Wuhan Fengtai Weiyuan Technology Co., Ltd. Resorcinol (99.0%) was bought from Shanghai Aladdin Biochemical Technology Co., Ltd. Acetylene black, polyvinylidene fluoride (PVDF), $LiPF_6$, ethylene carbonate (EC) and dimethyl carbonate (DMC) were purchased from Liyuan Battery Sales Department. All chemicals were used as received unless otherwise noted.

2.2. Synthesis of RT resin, HCs700 and HCs700@GPE

Firstly, 48 mL of deionized water [or 48 mL of GPE suspension (1 mg/mL)], 8 mL of anhydrous ethanol, and 0.3 mL of ammonia were added to a beaker in turn, and after mixing well, 0.4 g of resorcinol was added. After stirring for 30 min, 671 mL of 2-thenaldehyde was added to the system, which was sealed and placed in a constant temperature water bath at 40°C with magnetic stirring for 12 h to complete the pre-reaction. Next, the reacted solution was transferred to a hydrothermal reactor lined with polytetrafluoroethylene and placed in a tube furnace at 180°C for 24 hours. Finally, the reaction product was washed three times with deionized water, anhydrous ethanol, and acetone, and then dried in an oven at 100°C. The final orange-red product obtained was the RT resin (or GPE/RT resin composite). The molecular structure of RT resin was shown in Fig. 2.

The RT resin (or GPE/RT resin composite) obtained in the previous section was heated at 3 °C min^{-1} and kept at 700 °C under nitrogen atmosphere for 4 hours in a quartz tube furnace. Then it was cooled to the room temperature at the rate of 5 °C min^{-1} to obtain the hard carbon HCs700 (or HCs700@GPE).

2.3. Structural characterizations

The morphology of the above samples was examined by a Hitachi Su-70 scanning electron microscopy (SEM, Hitachi Inc., Tokyo, Japan). The dynamic light scattering (DLS) data was obtained by a laser particle size analyzer (MS 2000, Malvern Corporation, United Kingdom). The Fourier Transform Infrared (FT-IR) spectrum was performed by a NICOLET AVATAR 360 FTIR spectrometer. X-ray photoelectron spectroscopy (XPS) was detected by a ESCALAB 250Xi spectrometer. Thermogravimetric analysis (TG) and differential thermogravimetric analysis (DTG) were performed using a Netzsch STA 449 F3 Jupiter analyzer under a nitrogen atmosphere with the heating rate of 5°C per minute. Ultraviolet-visible (UV-vis) diffuse reflectance spectroscopy was characterized by a Shimadzu UV-2550 spectrophotometer. X-ray diffraction (XRD) was performed using a Kigaka D/max 2500 X-ray diffractometer (Cu-Ka as the radiation source, scan range of 5-80° (2θ), and scan rate of 5°/min). The nitrogen adsorption-desorption isotherms of the samples at 77.3 K were measured with an ASAP 2460-3 (Micromeritics) volumetric adsorption analyzer, and the specific surface area and porosity of the samples were determined.

2.4 Electrochemical measurements

PVDF binder, acetylene black, and the prepared active materials (RT resin or HCs700 or HCs700@GPE) were mixed into mortar in a mass ratio of 7:2:1, and then an appropriate amount of NMP solution was added to make a uniform slurry. After the slurry was coated on the copper foil, it was placed in a vacuum oven at 60° C for 24 hours and then cut into slices with a diameter of 12 mm to obtain the working electrode. 1.0 mol/L $LiPF_6$ was dissolved in the mixture of EC and DMC in a volume ratio of 1:1 to obtain the electrolyte solution. The working electrode, electrolyte solution, and lithium sheet were assembled into a CR2032 coin battery in a glove box filled with argon gas containing less than 0.1 ppm of water and oxygen.

Cyclic voltammetry (CV) measurements were performed with an Autolab PGSTAT302N electrochemical workstation (PGSTAT 128N, Metrohm) over the voltage range of 0.005-3.00 V at different scan rates. Galvanostatic charge-discharge (GCD) experiments were carried out at room temperature on a Wuhan Land Battery Testing System (LANDCT2001A). The electrochemical impedance spectroscopy (EIS) of the samples before cycling and after 300 cycles were measured using the Autolab PGSTAT302N (the scanning frequency from 100 kHz to 0.1 Hz and the perturbation voltage amplitude of 5 mV).

3. RESULTS AND DISCUSSION

3.1. Morphological characterization of the RT resin, HCs700, and HCs700@GPE

The morphologies of RT resin, HCs700, and HCs700@GPE were investigated by the SEM pictures as shown in Fig. 3a, 3c and 3d, respectively. Fig. 3a showed that all the RT polymer particles had smooth surface, good spherical shape, and uniform size. The DLS data (Fig. 3b) showed that the RT resin had good particle dispersion with a particle size around 517 nm. Fig. 3c showed that the spherical structure of HCs700 was intact but partially agglomerated. As can be seen from the SEM photograph of HCs700@GPE in Fig. 3d, GPE interspersed in the three-dimensional network structure formed by the stack of resin particles increased the electrode conductivity, thus improving the coulombic efficiency and electrochemical performance of the electrode [44].

3.2. FT-IR and XPS of the RT resin

Fig. 4 showed the FT-IR spectrum of RT resin. The peaks between 1038 and 1225 cm^{-1} can be assigned to the stretching vibration of the C-O-C [12]. The broad absorption band at 3457 cm^{-1} corresponded to the characteristic absorption of hydroxyl stretching vibration [45].

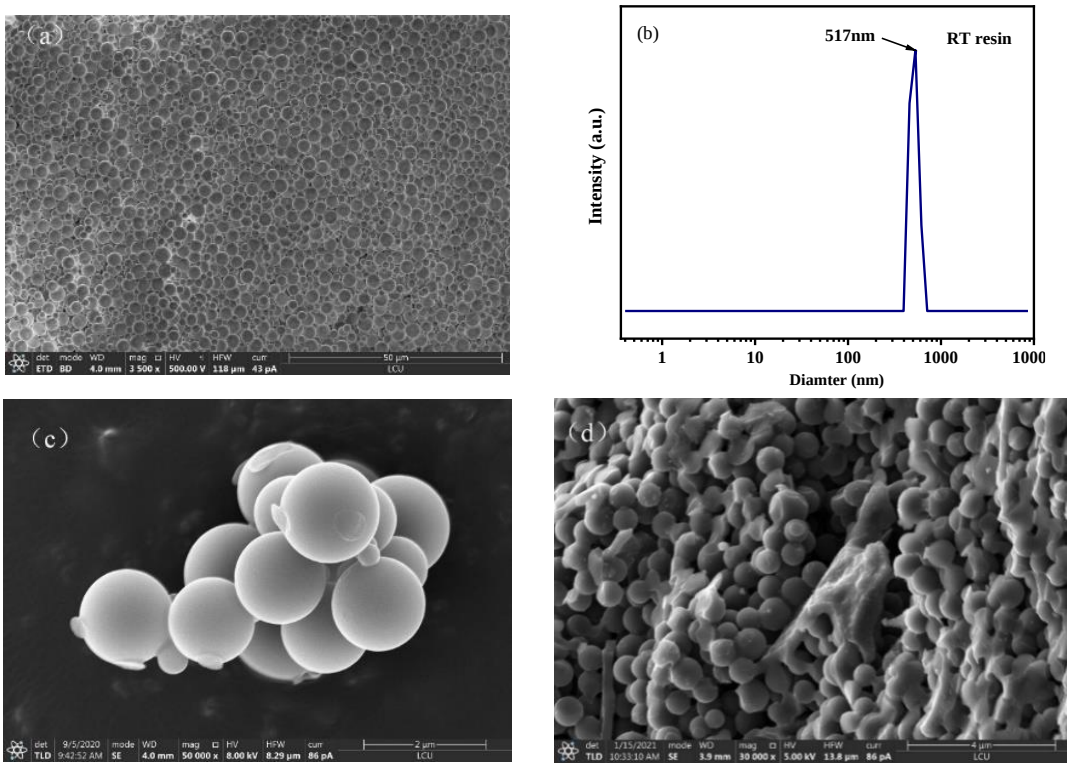

Figure 3. SEM imagines of (a) RT resin, (c)HCs700, and (d) HCs700@GPE. (b) DLS plot of the RT resin

The absorption peaks at 2865 and 2925 cm^{-1} can be attributed to the C-H stretching vibrations of the aromatic and thiophene rings [46]. The peaks at 1353 and 1464 cm^{-1} originated from the C=C stretching vibrations of the aromatic and thiophene rings [47]. The strong peaks near 733 and 794 cm^{-1} belonged to the C-H out-of-plane bending vibrations of the aromatic rings and thiophene units [2, 25]. The absorption peak at 1700 cm^{-1} was referred to the C=O stretching vibrations of the quinone derivates [26].

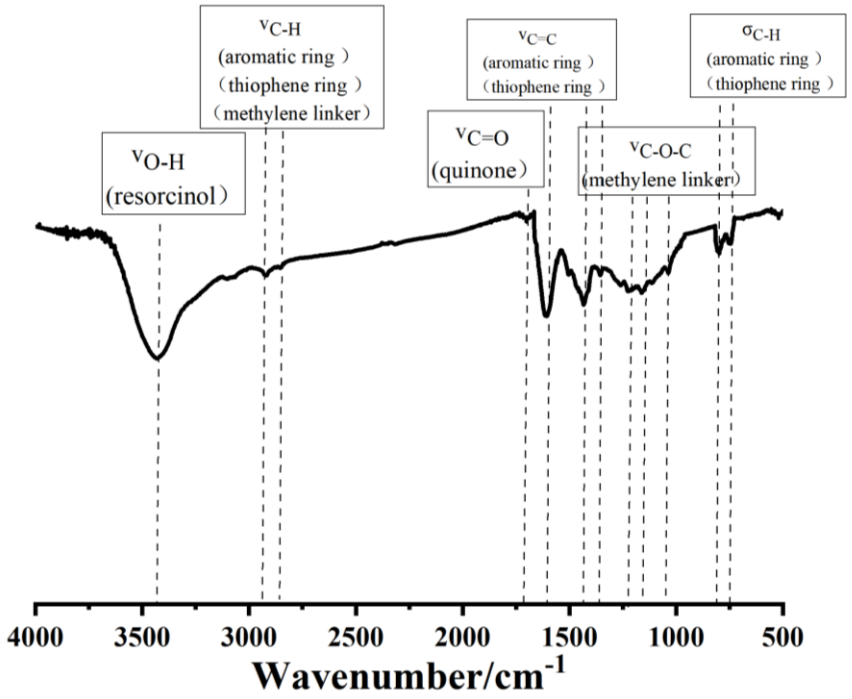

Figure 4. FT-IR spectrum of the RT resin

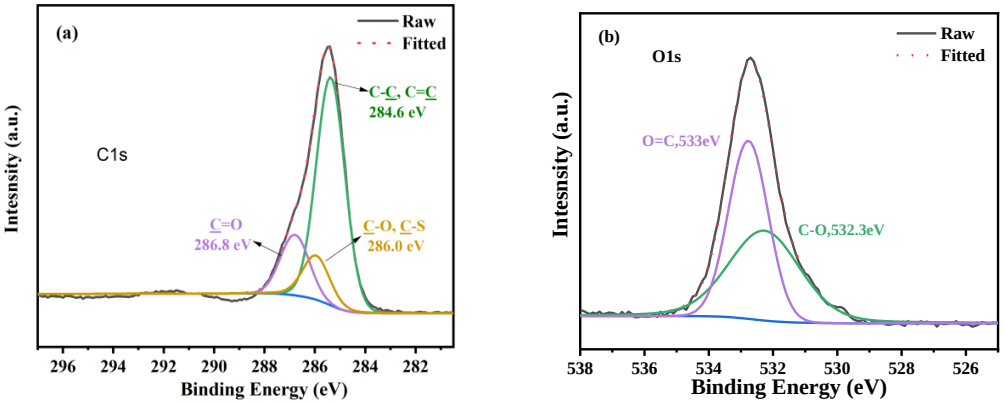

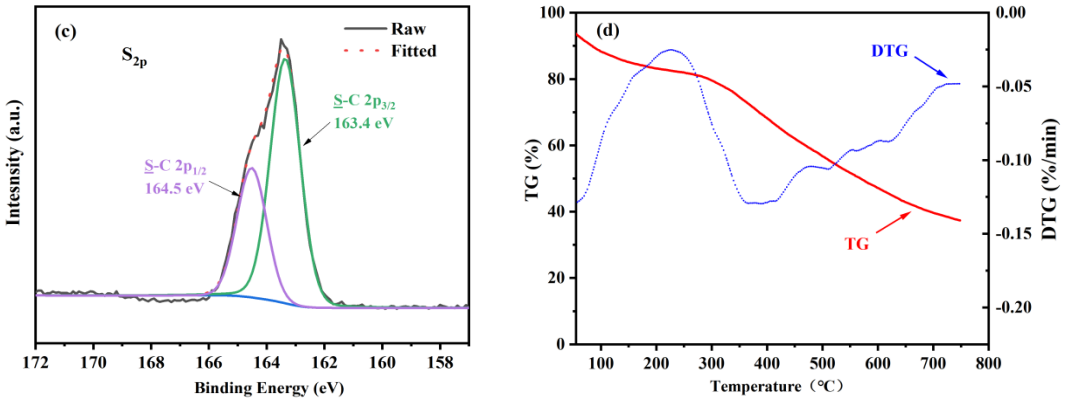

Figure 5. High-resolution XPS spectra of the RT resin: (a) C 1s, (b) O 1s, and (c) S 2p. (d) TG and DTG curves of the RT resin

X-ray photoelectron spectroscopy (XPS) was used to study the bonding conditions in the composites. The high-resolution C 1s, O 1s, and S 2p XPS spectra of the RT resin were shown in Fig. 5 a-5c, respectively. The C 1s peaks at 284.6 eV, 286.0 eV and 286.8 eV belonged to the C-C and C=C on the aromatic and thiophene ring, C-S on the thiophene unit, and C=O on the benzoquinone, respectively [48, 49]. In the O1s spectrum, the two peaks at 532.3 and 533.0 eV corresponded to the O-C on the benzene ring and O=C atoms on the benzoquinone unit, respectively [50, 51]. The splitting peaks of S 2p at 163.4 and 164.5 eV were associated with the $2p_{3/2}$ and $2p_{1/2}$ of S-C (on the thiophene ring), respectively [27].

3.3. TG and Energy level diagram of the RT resin

Fig. 5d showed the TG and DTG curves of the RT resin. The pyrolysis process of the RT resin can be divided into the following stages: in the first stage (before 150°C), the mass loss was about 15%, which was due to the evaporation of the solvent and water remaining in the sample; in the second stage (between 150°Cand 300°C), the mass loss was less; in the third stage (between 300°C and 800°C), the mass loss was about 40%, which was due to the charring of the resin and its carbon, hydrogen, oxygen and other elements became small molecular compounds (e.g., CH_4, CO_2, H_2O) and left the system [52]. The results showed that the RT resin was structurally stable until 300°C.

The E_g of the RT resin was measured through UV-vis diffuse reflectance spectroscopy in Fig. 6a. According to the Taucplot method [53], the E_g of the direct-band gap semiconductors can be calculated by Formula 1.

$$(\alpha hv)^{1/2}=K(hv-E_g) \quad (1)$$

where α is the absorption coefficient, h is the Planck constant, v is the vibration frequency, and K is a constant. As shown in Fig. 6b, the curve of $(\alpha hv)^{1/2}$ against hv was plotted and the linear portion of the curve was extrapolated to the horizontal axis with the intersection point being the value of E_g [25]. The E_g of the RT resin can be obtained as 1.85 eV, which was lower than that of the RF resin [26] as 2 eV, due to the fact that the former (D-D-A type conducting polymer) had one more electron donor unit

(i.e., thiophene) than the latter (D-A type polymer). The narrow E_g of RT resin indicated its good electrical conductivity and rate performance, making it suitable as an electrode material [24].

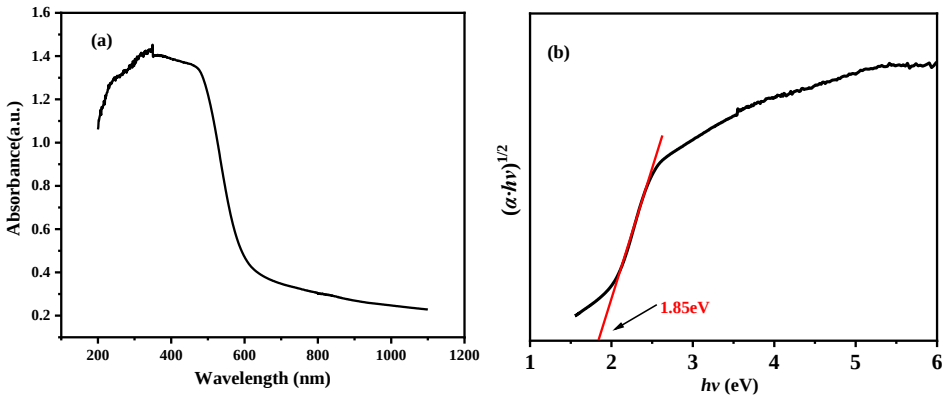

Figure 6. (a) UV-vis diffuse reflectance spectroscopy and (b) $(\alpha hv)^{1/2}$ *vs. hv* profiles of RT resin

3.4 Nitrogen adsorption-desorption isotherms and XRD of the RT resin, HCs700, and HCs700@GPE

As shown in Fig. 7a-c, the nitrogen adsorption-desorption isotherms of RT resin, HCs700, and HCs700@GPE corresponded to the type II, type IV, and type IV isotherm, respectively [54]. The specific surface area and average pore size were calculated using the Brunauer-Emmett-Teller (BET) and Barrett-Joyner-Halenda (BJH) methods, which were listed in Table 1. As shown, the specific surface area of HCs700 and HCs700@GPE was greatly enhanced compared to RT resin. Both the specific surface area and average pore size of HCs700@GPE were smaller than those of HCs 700, which can be attributed to the blocking of some channels of HCs 700 by the GPE [55].

Table 1. Specific surface area and average pore size of RT resin, HCs700, and HCs700@GPE

Sample	**RT resin**	**HCs700**	**HCs700@GPE**
Specific surface area(m^2/g)	8.5934	866.8527	584.3096
Average pore size(nm)	4.8190	4.3095	3.4516

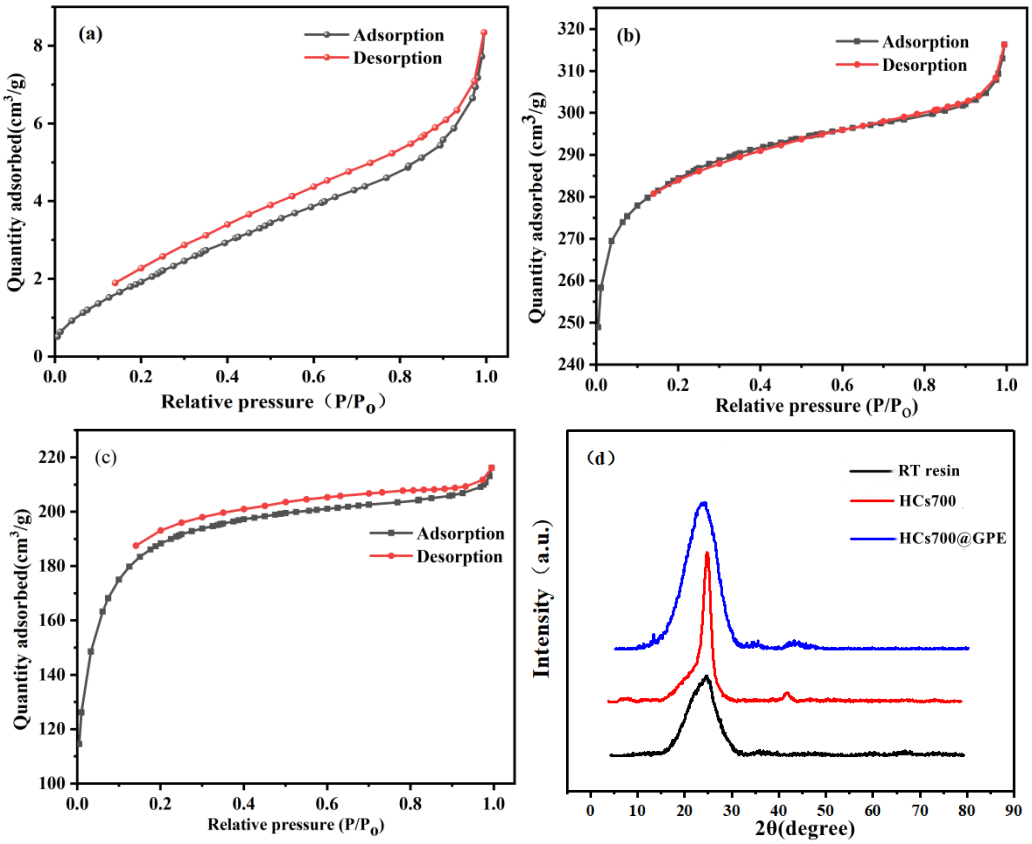

Figure 7. Nitrogen adsorption-desorption isotherms of (a) RT resin, (b)HCs700, and (c) HCs700@GPE. (d) XRD patterns of RT resin, HCs700, and HCs700@GPE

Fig. 7d showed the XRD patterns of RT resin, HCs700, and HCs700@GPE. All three had a diffraction peak at 2θ ≈ 23°, which was a typical feature of amorphous carbon [56]. Moreover, both HCs700 and HCs700@GPE had a small diffraction peak at 2θ≈43°, originating from the graphite crystallites formed during the carbonization of RT resin [12].

3.5 EIS measurements

Fig. 8 showed the Nyquist plots of RT resin, HCs700, and HCs700@GPE before cycling and after 300 cycles, where the inset was the equivalent circuit diagram. It can be seen that the Nyquist plots for all three samples consisted of a fuzzy semicircle in the high-frequency region, a semicircle in the mid-frequency region, and a diagonal line in the low-frequency region [57]. The fuzzy semicircle in the high frequency region was related to the transport process at the interface between the a solid electrolyte interfacial (SEI) film and the electrode [58]. The arc in the low and middle frequency corresponded to the charge transfer resistance and capacitance impedance between the composite electrode and the electrolyte [25, 27]. The diagonal line in the low frequency corresponded to the diffusion -controlled process, which was caused by the so-called Warburg impedance [59]. The Nyquist plots of the three materials can be fitted and analyzed according to the equivalent circuit model (inset in Fig. 8a). The R_{Ω} referred to the Ohmic resistance of the cell, including the resistance of the electrolyte and the electrode itself [4]. Q_{SEI} and R_{SEI} represented the capacitance and resistance of the SEI film [59], respectively. Q_d

and R_{ct} denoted the capacitance and charge transfer resistance between the composite and the electrolyte [6], respectively. Q_w represented the diffusion impedance of lithium ions in the solid [25, 60, 61]. The value of R_{ct} can be obtained by fitting the equivalent circuit model. Before cycling, the R_{ct} values of RT resin, HCs700, and HCs700@GPE were 300Ω, 231.3Ω, and 110.4Ω, respectively. While after 300 cycles, the R_{ct} values of all the three samples decreased to 155.2Ω, 107.8Ω, and 87.4Ω, respectively, due to the continuous activation of the electrodes during the charge and discharge process [54].

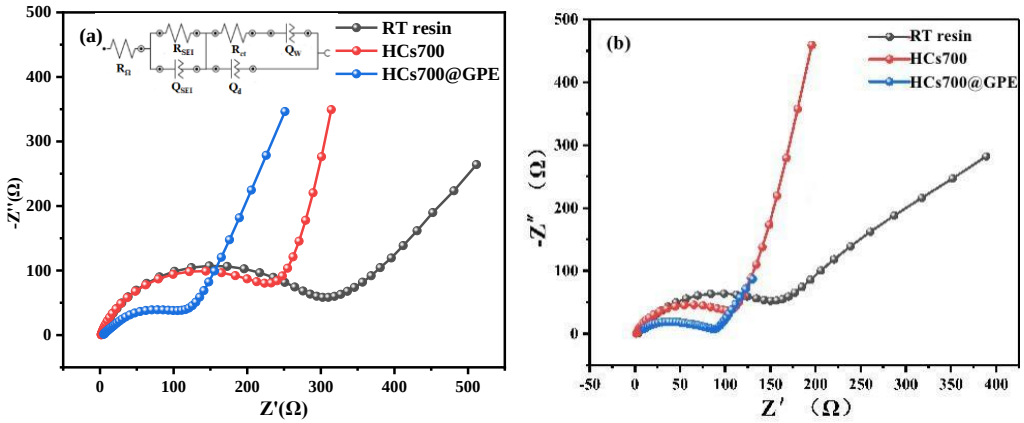

Figure 8. Nyquist plots of RT resin, HCs700, and HCs700@GPE (a) before cycling, and (b) after 300 cycles

3.6 CV, GCD, cycling stability, and rate performance

The CV curves of the RT resin were shown in Fig. 9a. It can be seen that the shape of the CV curve for the first cycle was different from that of the two subsequent cycles, especially during the discharge process. In the first cycle, two strong cathodic peaks were observed at 0.6 and 1.0 V (but disappeared in the subsequent cycles) due to the formation of SEI film by irreversible decomposition of the electrolyte [62]. The formation of SEI film led to a higher irreversible capacity and a lower initial coulombic efficiency in the first cycle. In the subsequent cycles, the CV curves of the RT resin almost overlapped, indicating the good reversibility of the electrode reaction [48].

Fig. 9b, Fig. 9c, and Fig. 9d showed the GCD curves of the RT resin, HCs700, and HCs700@GPE at the current density of 100 mA g^{-1}, respectively. The cycling stability curves of the three samples at the current densities of 100 mA g^{-1} and 500 mA g^{-1} were shown in Fig. 9e and Fig. 9f, respectively. The initial discharge capacity of the three electrode materials in the first cycle was 301.4, 1007.3, and 975.8 mAh g^{-1}, respectively. The initial charge capacity of the three electrodes was much lower compared to the initial discharge capacity, leading to a low coulombic efficiency in the first cycle (Fig. 9e and Fig. 9f). This phenomenon can be attributed to the formation of SEI film [63] and the decomposition of the electrolyte [64], which was similar for many electrode materials [65]. However, as shown in Fig. 9e and Fig. 9f, the coulomb efficiency of the three electrodes increased to more than 80% in the second cycle, and remained close to 100% in the subsequent cycles. The results showed that the three electrodes had good cycling stability, which was consistent with the results of CV experiments.

It can be seen from Fig. 9e and Fig. 9f that the specific capacity of the three samples gradually increased with charging and discharging, which was related to the electrochemical activation of the electrode [64] (i.e., the electrolyte solution continuously entered the interior of the electrode as the lithium ions were continuously embedded and de-embedded inside the electrode material [57], leading to an increase in the active sites inside the electrode [49]). As shown in Fig. 9e, after 300 cycles, the capacities of RT resin, HCs700, and HCs700@GPE at the current density of 100 mA g^{-1} were 270.1, 596.6, and 462.8 mAh g^{-1}, respectively, while as shown in Fig. 9f, after 600 cycles, their capacities at the current density of 500 mA g^{-1} were 210.2, 440.7, and 291.8 mAh g^{-1}, respectively.

The specific capacity of RT resin (270.1 mAh g^{-1} at 100 mA g^{-1}) was apparently higher than that of RF resin (145 mAh g^{-1} at 100 mA g^{-1}) [34-38], which was attributed to the extra one more electron donor unit (i.e., thiophene) in the RT resin molecule. The introduction of the thiophene unit led to RT resin with a narrower band gap (Eg: 1.85 eV vs. 2 eV), better redox properties, and ultimately a higher specific capacity [27, 39-41]. As shown in Table 2, the specific capacity of RT resin-derived hard carbon (HCs700) prepared in this paper was all higher than the RF resin-derived hard carbon reported in the literature, which was due to the fact that the N doping in HCs700 greatly improved the electrochemical properties of the carbon material and greatly increased the number of active sites for lithium-ion reaction [42, 43].

The specific capacity of HCs700 and HCs700@GPE was obviously better than that of RT resin, because the specific surface area of the former was much larger than that of the latter. (The larger the specific surface area of the electrode, the more reaction sites are exposed to the electrolyte and the larger the specific capacity of the electrode[48]). The flatter cycling stability curve means the better cycling stability of the electrode. So, it can be seen from Fig. 9e and 9f that the cycling stability of HCs700@GPE was better than that of HCs700, which may be due to the fact that the GPE provided a good conductive network for the hard carbon and improved the electrical conductivity of the electrode.

Table 2 Comparison of specific capacity of RT and RF resin-derived hard carbon

Sample	Specific capacity (mAh g^{-1})	Current density	Reference
HCs700	596.6	100 mA g^{-1}	This work
Carbon xerogel nanoparticles derived from RF resin	385	37.2 mA g^{-1}	[37]
Carbon aerogels prepared derived from RF resin	333	50 mA g^{-1}	[66]
Nitrogen-doped carbon xerogels derived from RF resin	280	37.2 mA g^{-1}	[67]

Hard carbon microspheres derived from RF resin	321	0.1 C	[68]
Composite of SiO, and carbon xerogel derived from RF resin	547	100 mA g^{-1}	[38]
Carbon aerogels derived from RF resin	333	50 mA g^{-1}	[66]

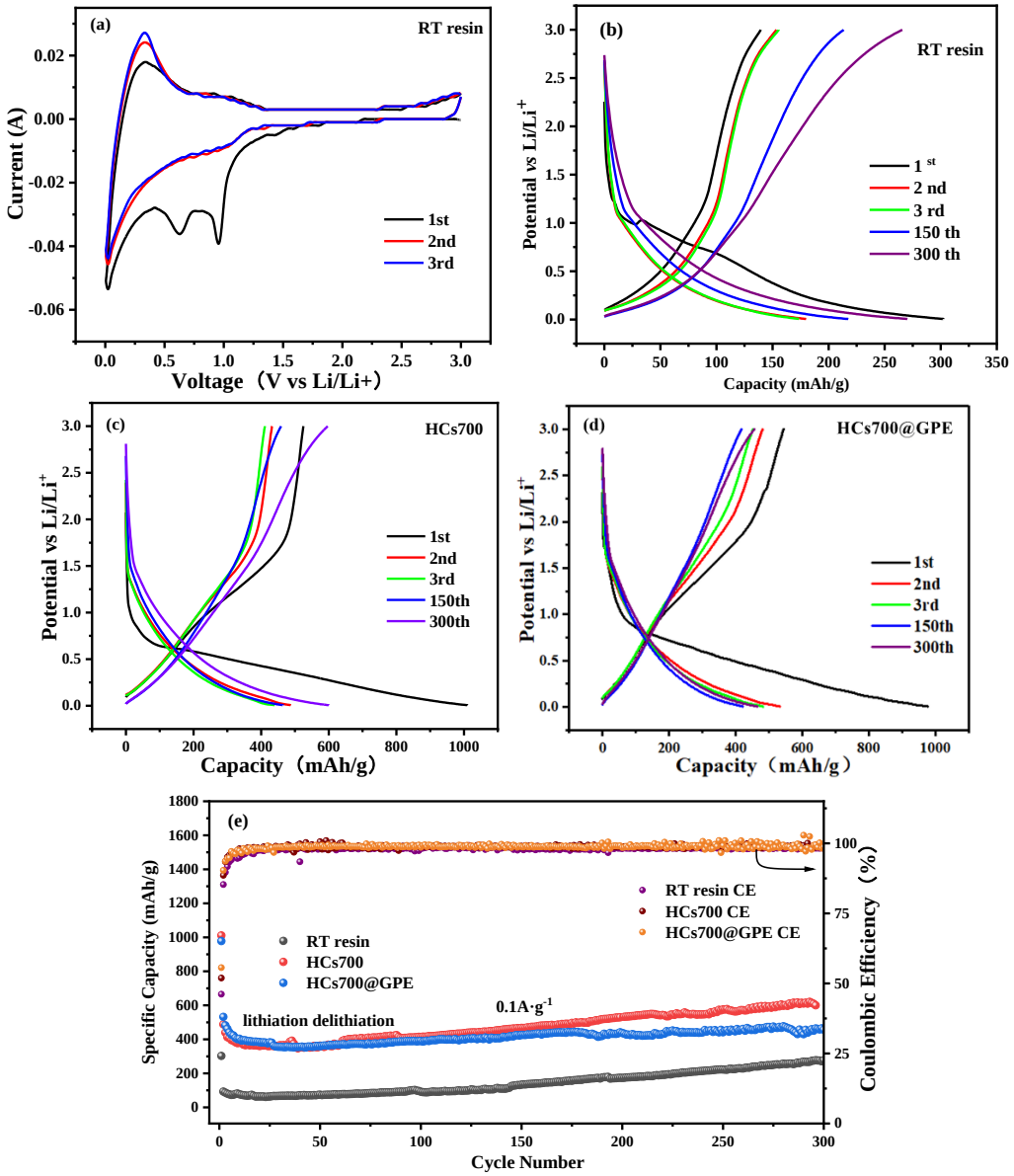

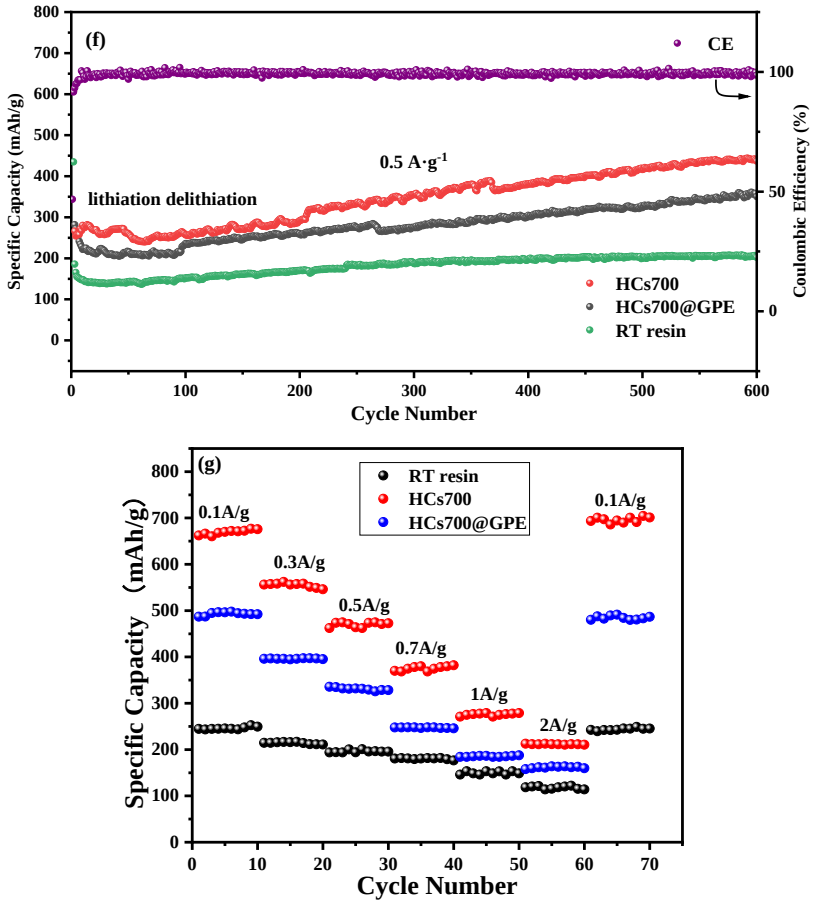

Figure 9. (a) CV curves of the RT resin at the scan rate of 0.1 mV s^{-1}.GCD curves at the current density of 100 mA g^{-1} of (b) RT resin, (c) HCs700, and (d) HCs700@GPE. Cycling stability curves of the three samples at the current density of (e) 100 mA g^{-1} and (f)500 mA g^{-1}. (g) Rate performance of the three samples.

The rate performance of the three samples were conducted at different current densities (0.1, 0.3, 0.5, 0.7, 1, and 2 A g^{-1}), as shown in Fig. 9g. The ability to maintain stable cycling performance during rapid changes in the charging and discharging rate is an important indicator to characterize the rate performance of the electrode [25]. As can be seen, the specific capacity of the three samples decreased as the current density increased from 0.1 A g^{-1} to 2 A g^{-1}, and then when the current density returned to 0.1 A g^{-1}, all the three materials could be restored to their respective original levels, indicating that all the three electrode materials had good rate performance [48]. Although the specific capacity of HCs700 was larger than that of HCs700@GPE at the same current density, the fluctuation of the former was significantly smaller than the latter, indicating that the rate performance of HCs700@GPE was better because the GPE in HCs700@GPE improved the conductivity of the electrode.

4. CONCLUSION

In order to further improve the electrochemical properties of the resorcinol-formaldehyde (RF) resin and its derived hard carbon, this paper reported a D-D-A type RT resin synthesized by high temperature hydrothermal synthesis using resorcinol and 2-thenaldehyde as raw materials.

The specific capacity of RT resin (270.1 mAh g^{-1} at 100 mA g^{-1}) was apparently higher than that of RF resin (145 mAh g^{-1} at 100 mA g^{-1}) which was attributed to the extra one more electron donor unit (i.e., thiophene) in the RT resin molecule. The introduction of the thiophene unit led to RT resin with a narrower band gap (E_g: 1.85 eV vs. 2 eV), better redox properties, and ultimately a higher specific capacity. Furthermore, the specific capacity of RT resin-derived hard carbon (HCs700) prepared in this paper was all higher than the RF resin-derived hard carbon reported in the literature, which was due to the fact that the N doping in HCs700 greatly improved the electrochemical properties of the carbon material and greatly increased the number of active sites for lithium-ion reaction.

At the current density of 100 mA g^{-1}, the discharge capacities of RT resin, HCs700, and HCs700@GPE were 301.4, 1007.3 and 975.8 mAh g^{-1} at the first cycle, respectively, and remained around 270.1, 596.6 and 462.8 mAh g^{-1} after 300 cycles, respectively. The specific capacity of HCs700 and HCs700@GPE was obviously better than that of RT resin, because the specific surface area of the former was much larger than that of the latter. Although the specific capacity of HCs700 was larger than that of HCs700@GPE at the same current density, the fluctuation of the former was significantly smaller than the latter, indicating that the rate performance of HCs700@GPE was better because the GPE in HCs700@GPE improved the conductivity of the electrode. The prepared HCs700 and HCs700@GPE electrode materials had good specific capacity and rate performance, which were well suited as anode materials for LIBs.

CRediT authorship contribution statement

Qing Lu: Data analysis, Writing (original draft). Lingqian Kong: Writing - review & editing. Bo Liang: Writing - review & editing. Jinsheng Zhao: Data analysis.

DECLARATION OF COMPETING INTEREST

The authors declare that they have no known competing financial interests or personal relationships that could have appeared to influence the work reported in this paper.

ACKNOWLEDGEMENTS

The work was financially supported by the National Natural Science Foundation of China (51473074, 21601079), Heilongjiang Provincial Natural Science Foundation of China (LH2020E089), Basic Scientific Research program of Nantong City (JC22022014), Outstanding young core teachers from "Green-Blue Project" of Colleges and Universities in Jiangsu Province, China Postdoctoral Science Foundation (2021M691970), Postdoctoral Innovation Project of Shandong Province (202103051), and University Nursing Program for Young Scholars with Creative Talents in Heilongjiang Province (UNPYSCT-2018205).

References

1. Y. Liang, Z. Tao and J. Chen, *Adv. Energy. Mater.*, 2 (2012) 742.
2. B. Moeremans, H.-W. Cheng, Q. Hu, H.F. Garces, N.P. Padture, F.U. Renner and M. Valtiner, *Nat. Commun.*, 7 (2016) 1.

3. C. Zhang, Y. He, P. Mu, X. Wang, Q. He, Y. Chen, J. Zeng, F. Wang, Y. Xu and J.X. Jiang, *Adv. Funct. Mater.*, 28 (2018) 1705432.
4. C. Wu, M. Hu, X. Yan, G. Shan, J. Liu and J. Yang, *Energy Stor. Mater.*, 36 (2021) 347.
5. K.M. Tsang and W.L. Chan, *Energ. Convers. Manage.*, 52 (2011) 1593.
6. X.-Y. Song, Y.-H. Zhang, P.-P. Sun, J. Gao and F.-N. Shi, *Chem. Eur. J.*, 26 (2020) 5654.
7. M. Armand, S. Grugeon, H. Vezin, S. Laruelle, P. Ribière, P. Poizot and J.M. Tarascon, *Nat. Mater.*, 8 (2009) 120.
8. M.E. Bhosale, S. Chae, J.M. Kim and J.-Y. Choi, *J. Mater. Chem. A*, 6 (2018) 19885.
9. A.S. Aric, P. Bruce, B. Scrosati, J.M. Tarascon and W.V. Schalkwijk, *Nat. Mater.*, 4 (2005) 366.
10. G. Peng, A. Wang, X. Wang and Z. Tao, *Catal. Lett.*, 125 (2008) 289.
11. L.L. Hench and J.K. West, *Chem. Rev.*, 90 (1990) 33.
12. R.W. Pekala, *J. Mater. Sci.*, 24 (1989) 3221.
13. T. Yokoi, Y. Sakamoto, O. Terasaki, Y. Kubota, T. Okubo and T.J.J.a.c.s. Tatsumi, *J. Am. Chem. Soc*, 128 (2006) 13664.
14. J.S. Carter, S. Kramer, J.J. Talley, T. Penning, P. Collins, M.J. Graneto, K. Seibert, C.M. Koboldt, J. Masferrer and B. Zweifel, *Biorg. Med. Chem. Lett.*, 9 (1999) 1171.
15. C.V. Loricera, B. Pawelec, A. Infantes-Molina, M. Álvarez-Galván, R. Huirache-AcuA, R. Nava and J. Fierro, *Catal. Today*, 172 (2011) 103.
16. C. Yu, B. Tian, J. Fan, G.D. Stucky and D. Zhao, *J. Am. Chem. Soc.*, 124 (2002) 4556.
17. F. Zhang, D. Gu, T. Yu, F. Zhang, S. Xie, L. Zhang, Y. Deng, Y. Wan, B. Tu and D. Zhao, *J. Am. Chem. Soc.*, 129 (2007) 7746.
18. C. Peng, G.H. Ning, S. Jie, G. Zhong and K.P. Loh, *Nat. Energy*, 2 (2017) 17074.
19. K. Oyaizu, W. Choi and H. Nishide, *Polym. Adv. Technol.*, 22 (2011) 1242.
20. Z. Song, H. Zhan and Y. Zhou, *Angew. Chem. Int. Ed.*, 49 (2010) 8444.
21. H.X. Zhang, C. Feng, Y.C. Zhai, K.L. Jiang, Q.Q. Li and S.S. Fan, *Adv. Mater.*, 21 (2009) 2299.
22. Z.-S. Wu, W. Ren, L. Xu, F. Li and H.-M. Cheng, *ACS nano*, 5 (2011) 5463.
23. F. Ding, W. Xu, D. Choi, W. Wang, X. Li, M.H. Engelhard, X. Chen, Z. Yang and J.-G. Zhang, *J. Mater. Chem.*, 22 (2012) 12745.
24. T. Marszalek, M. Li and W. Pisula, *Chem. Commun.*, 52 (2016) 10938.
25. X. Xue, J. Luo, L. Kong, J. Zhao, Y. Zhang, H. Du, S. Chen and Y. Xie, *RSC Adv.*, 11 (2021) 10688.
26. Y. Shiraishi, T. Takii, T. Hagi, S. Mori, Y. Kofuji, Y. Kitagawa, S. Tanaka, S. Ichikawa and T. Hirai, *Nat. Mater.*, 18 (2019) 985.
27. B. Liang, X. Liu, X. Guo and J. Zhao, *Synth. Met.*, 289 (2022) 117112.
28. C. Li, X. Guo, H. Du, J. Zhao, L. Liu, Q. Yuan and C. Fu, *J. Solid State Electrochem.*, 25 (2021) 1847.
29. H. Shi, *Electrochim. Acta*, 41 (1996) 1633.
30. U. Jeong, Y. Wang, M. Ibisate and Y. Xia, *Adv. Funct. Mater.*, 15 (2005) 1907.
31. Y. Wu, E. Rahm and R. Holze, *J. Power Sources*, 114 (2003) 228.
32. S. Wang and Q. Liu, *Chin. J. Chem. Eng.*, 22 (2000) 533.
33. J. Lu, Y. Jin and S. Xiao, *New Chem. Mater.*, 42 (2014) 109.
34. M.M. Gaikwad, M. Kakunuri and C.S. Sharma, *Mater. Today Commun.*, 20 (2019) 100569.
35. M. Kakunuri and C.S. Sharma, *J. Mater. Res.*, 33 (2018) 1074.
36. M. Suresh, M. Kakunuri and C.S. Sharma, *ECS Trans.*, 77 (2017) 331.
37. M. Kakunuri, S. Vennamalla and C.S. Sharma, *RSC Adv.*, 5 (2015) 4747.
38. X. Yuan, Y.-J. Chao, Z.-F. Ma and X. Deng, *Electrochem. Commun.*, 9 (2007) 2591.
39. Q. Pei, G. Zuccarello, M. Ahlskog and O. Inganäs, *Polymer*, 35 (1994) 1347.
40. X. Chen, H. Zhang, C. Ci, W. Sun and Y. Wang, *ACS Nano*, 13 (2019) 3600.
41. X. Guo, Q. Yuan, C. Li, H. Du, J. Zhao, L. Liu, Y. Li, Y. Xie and V. Vaidya, *RSC Adv.*, 11 (2021) 15044.

42. W. Guo, X. Li, J. Xu, H.K. Liu, J. Ma and S.X. Dou, *Electrochim. Acta*, 188 (2016) 414.
43. C. Qian, P. Guo, X. Zhang, R. Zhao, Q. Wu, L. Huan, X. Shen and M. Chen, *RSC Adv.*, 6 (2016) 93519.
44. X. Zhang, H. Zhang, C. Li, K. Wang, X. Sun and Y. Ma, *RSC Adv.*, 4 (2014) 45862.
45. D. Wu, R. Fu and Z. Yu, *J. Appl. Polym. Sci.*, 96 (2010) 1429.
46. S. Xu, J. Zhou, J. Wang, S. Pathiranage, N. Oncel, P. Robert Ilango, X. Zhang, M. Mann and X. Hou, *Adv. Funct. Mater.*, 31 (2021) 2101645.
47. M. Wilson, *J. Soil Sci.*, 32 (1981) 167.
48. Q. Yuan, C. Li, X. Guo, J. Zhao, Y. Zhang, B. Wang, Y. Dong and L. Liu, *Energy Rep.*, 6 (2020) 2094.
49. Z. Du, W. Ai, L. Xie and W. Huang, *J. Mater. Chem. A*, 2 (2014) 9164.
50. Y. Liu, Y. Qiao, W.-X. Zhang, Z. Li, X.-L. Hu, L.-X. Yuan and Y.-H. Huang, *J. Mater. Chem.*, 22 (2012) 24026.
51. L. Qie, W.-M. Chen, Z.-H. Wang, Q.-G. Shao, X. Li, L.-X. Yuan, X.-L. Hu, W.-X. Zhang and Y.-H. Huang, *Adv. Mater.*, 24 (2012) 2047.
52. G. Biesmans, A. Mertens, L. Duffours, T. Woignier and J. Phalippou, *J. Non-Cryst. Solids*, 225 (1998) 64.
53. K. Hultzsch, *Eur. J. Inorg. Chem.*, 74 (1941) 1539.
54. X. Yang and A.L. Rogach, *Adv. Energy. Mater.*, 9 (2019) 1900747.
55. D. Hou, Z. Xu, Z. Yang, C. Kuai, Z. Du, C.-J. Sun, Y. Ren, J. Liu, X. Xiao and F. Lin, *Nat. Commun.*, 13 (2022) 1.
56. L. Zhan, Z. Song, J. Zhang, J. Tang, H. Zhan, Y. Zhou and C. Zhan, *Electrochim. Acta*, 53 (2008) 8319.
57. B. Ni, Y. Li, T. Chen, T. Lu and L. Pan, *J. Colloid Interface Sci.*, 542 (2019) 213.
58. X. Liu, L. Kong, H. Du, Y. Zhang, J. Zhao and Y. Xie, *Org. Electron.*, 64 (2018) 223.
59. G. Zhang, Z. Xu, P. Liu, Y. Su, T. Huang, R. Liu, X. Xi and D. Wu, *Electrochim. Acta*, 260 (2018) 598.
60. P. Hu, H. Wang, Y. Yang, J. Yang, J. Lin and L. Guo, *Adv. Mater.*, 28 (2016) 3486.
61. Z.L. Yu, S. Xin, Y. You, Y. Le, Y. Lin, D.W. Xu, C. Qiao, Z.H. Huang, Y. Ning and S.H. Yu, *J. Am. Chem. Soc.*, 138 (2016) 14915.
62. N.A. Banek, K.R. McKenzie, D.T. Abele and M.J. Wagner, *Sci. Rep.*, 12 (2022) 1.
63. C. Li, L. Kong, J. Zhao and B. Liang, *Colloids Surf. Physicochem. Eng. Aspects*, 651 (2022) 129707.
64. H. Kang, H. Liu, C. Li, L. Sun, C. Zhang, H. Gao, J. Yin, B. Yang, Y. You, K.-C. Jiang, H. Long and S. Xin, *ACS Appl. Mater. Interfaces*, 10 (2018) 37023.
65. H. Buqa, A. Wuersig, J. Vetter, M.E. Spahr, F. Krumeich and P. Novak, *J. Power Sources*, 153 (2006) 385.
66. N.-P. Liu, J. Shen, D.-Y. Guan, D. Liu, X.-W. Zhou and Y.-J. Li, *Acta Phys-Chim. Sin.*, 29 (2013) 966.
67. X. Liu, S. Li, J. Mei, W.-M. Lau, R. Mi, Y. Li, H. Liu and L. Liu, *J. Mater. Chem. A*, 2 (2014) 14429.
68. Q. Zhang, X. Deng, M. Ji, Y. Li and Z. Shi, *Ionics*, 26 (2020) 4523